Microscopic dynamics of lithium diffusion in single crystal of the solid-state electrolyte La$_{2/3-x}$Li$_{3x}$TiO$_3$ ($x = 0.13$) studied by quasielastic neutron scattering

Masato Matsuura ,[1,*] Yasuyuki Fujiwara,[2] Hiroki Moriwake,[3] Koji Ohara,[4] and Yukinobu Kawakita[5]

[1]*Neutron Science and Technology Center, Comprehensive Research Organization for Science and Society (CROSS), Tokai, Ibaraki 319-1106, Japan*
[2]*Faculty of Engineering, Shinshu University, Wakasato, Nagano 380-8533, Japan*
[3]*Nanostructures Research Laboratory, Japan Fine Ceramics Center, Nagoya, Aichi 456-8587, Japan*
[4]*Diffraction and Scattering Division, Center for Synchrotron Radiation Research, Japan Synchrotron Radiation Research Institute (SPring-8/JASRI), Sayo, Hyogo 679-5198, Japan*
[5]*J-PARC Center, Japan Atomic Energy Agency, Tokai, Ibaraki 319-1195, Japan*

Quasielastic neutron scattering (QENS) measurements combined with first principles based molecular-dynamics calculations were conducted to study the dynamics of Li$^+$ ions in a solid-state electrolyte La$_{2/3-x}$Li$_{3x}$TiO$_3$ (LLTO) with $x = 0.13$. By using a large ^{7}Li-enriched single crystal sample, a QENS signal was clearly observed along the three principal axes [110], [111], and [001] at a temperature (T) of 600 K. Wave vector dependence of the linewidth of the QENS signal along each direction was explained well using the Chudley-Elliot model for jumps between the A sites of the perovskite lattice through the bottleneck square, which was also supported by molecular dynamics calculations. At $T = 600$ K, the estimated self-diffusion coefficient of Li$^+$ (D_{Li}) in the ab plane [$D_{Li}^{ab} = (6.8 \pm 0.5) \times 10^{-6}$ cm^2/s] was slightly larger than that along the c axis [$D_{Li}^c = (4.4 \pm 0.3) \times 10^{-6}$ cm^2/s], suggesting quasi-isotropic diffusion, that is, the three-dimensional diffusion of Li$^+$ ions. The decrease in D_{Li} with decreasing T was reasonably explained by a thermal activation process with the activation energy determined from ionic-conductivity measurements. Furthermore, the estimated values of the self-diffusion coefficient of Li$^+$ ions are comparable to those in the sulfide-based Li$^+$ ion conductor, Li$_7$P$_3$S$_{11}$, although its ionic conductivity is 10 times larger than that for LLTO. The obtained microscopic information on Li$^+$ diffusion in LLTO clarifies how to understand the Li conduction mechanism in LLTO and Li$_7$P$_3$S$_{11}$ in a unified manner and can provide a way to increase the Li$^+$ ionic conductivity in oxide-based solid electrolytes.

I. INTRODUCTION

An all-solid-state lithium-ion battery has been heavily investigated as a next-generation energy storage system [1,2], because both the energy density and safety of such all-solid-state batteries are expected to be drastically improved by replacing an organic solvent-based liquid electrolyte with a solid electrolyte. Sulfide-based Li$^+$ ionic conductors, such as Li$_{10}$GeP$_2$S$_{12}$ (LGPS), are considered to be promising candidates for a solid electrolyte because of their extremely high Li$^+$ ionic conductivity (σ_{Li}) ranging approximately 10^{-2} S/cm at room temperature, which is comparable to the σ_{Li} of typical liquid electrolytes [3]. By contrast, σ_{Li} of oxide-based Li$^+$ ionic conductors is more than one order of magnitude lower than that of sulfide-based Li$^+$ ionic conductors such as LGPS, Li$_3$PS$_4$, and Li$_7$P$_3$S$_{11}$, as summarized in Table I. Because oxide-based Li$^+$ ionic conductors have an excellent stability in air, it is highly desirable to develop oxide-based Li$^+$ ionic conductors with a high σ_{Li}.

Among the many oxide-based Li$^+$ ionic conductors, La$_{2/3-x}$Li$_{3x}$TiO$_3$ (LLTO) exhibits the highest σ_{Li} at room tem-

perature [4–6]. Since LLTO poses a simple double-perovskite structure [see Fig. 1(a)], LLTO is considered an ideal system for studying the relationship between the Li$^+$ conduction mechanism and structural properties in solids. Previous extensive structural studies on LLTO revealed the following key features on σ_{Li} [5,7–13]. First, σ_{Li} is closely related to the La and defect contents at the A site in a double-perovskite lattice, in which the La-rich and La-poor layers are stacked alternately along the c axis. Li$^+$ ions mainly conduct through the La-poor layer, when the Li concentration is low (or $x < 0.08$) [5,9–12]. The difference in the La occupancy between the La-rich and La-poor layers decreases with the Li content. A nearly three-dimensional diffusion is expected for an Li-rich composition. Second, σ_{Li} strongly depends on the size of the "bottleneck" square surrounded by oxygen ions. The potential barrier of σ_{Li} is dominated by the repulsion energy from oxygen ions [11,13].

Unfortunately, these findings are based on the time-averaged structure and do not provide direct information on the dynamics of Li$^+$ ions. However, neutron scattering can detect the motion of Li$^+$ ions as quasielastic neutron scattering (QENS). When a neutron is scattered by a mobile Li$^+$ ion, neutron energy is transferred to, or from, the Li$^+$ ions, resulting in broadening of the elastic signal. The wave vector (Q)

---

*m_matsuura@cross.or.jp

TABLE I. Comparison of ionic conductivity (σ_{Li}), activation energy (E_a), and diffusion coefficient (D_{Li}) for LGPS, Li_3PS_4, $Li_7P_3S_{11}$ (glass), and LLTO. σ_{Li} and E_a are the values at room temperature (RT). D_{Li}'s for LGPS and Li_3PS_4 are the reported values obtained from pulsed field gradient nuclear magnetic resonance measurements, whereas D_{Li}'s for $Li_7P_3S_{11}$ and LLTO are obtained from QENS measurements.

Systems	σ_{Li} (S/cm)	E_a (eV)	D_{Li} (cm^2/s)
LGPS	1.2×10^{-2} [3]	0.25 [3]	$3 \times 10^{-8} (RT)$ [14] $6 \times 10^{-7} (T = 473\,K)$
Li_3PS_4	2×10^{-4} [15]	0.35 [15]	9×10^{-10} (RT) [16] $2.9 \times 10^{-8} (T = 473\,K)$[a]
$Li_7P_3S_{11}$ (glass)	0.91×10^{-3} [17]	0.44 [17]	$5.7 \times 10^{-6} (T = 473\,K)$ [18]
LLTO	7×10^{-5} [5]	$0.4 (T < 400\,K)$, $0.15 (T > 400\,K)$ [5]	$6.8 \times 10^{-6} (T = 600\,K)$,[a] $3.1 \times 10^{-6} (T = 473\,K)$

[a]D_{Li} at $T = 473$ K for Li_3PS_4 and LLTO are estimated using the Arrhenius law with E_a.

dependence of the linewidth of the QENS provides detailed information on the dynamical conduction path of Li$^+$ on a microscopic scale, such as the residence time (τ) and jump vector (l). Furthermore, if a single crystal is available, directional information of Li$^+$ jump can be obtained. However, such a detailed QENS study using a single crystal has not been reported thus far, perhaps owing to a lack of sufficiently large single crystals and weak QENS signals from mobile Li$^+$ ions.

In this paper, we present a QENS study on the dynamics of Li$^+$ ions using a single crystal of LLTO and a state-of-the-art neutron backscattering spectrometer. Combined with a molecular dynamics (MD) simulation using first-principles calculations, the dynamical conduction path and direction dependent self-diffusion coefficient of Li$^+$ ions (D_{Li}) at a microscopic scale have been directly extracted from QENS data.

II. EXPERIMENTAL DETAILS

A powder sample of ^{7}Li-enriched LLTO was synthesized using a solid-state reaction technique for the stoichiometric mixtures of ^{7}Li-enriched Li_2CO_3 (99.9%, Cambridge Isotope Laboratories, Inc.), La_2O_3 (99.9%, Miike Smelting Co., Ltd.), and TiO_2 (99.9%, Toho Titanium Co., Ltd.). The quality of the obtained LLTO powder was confirmed by powder x-ray diffraction measurements (SmartLab, Rigaku Corporation), as shown in Fig. S1 in the Supplemental Material [19]. Bulk single crystals of ^{7}Li-enriched LLTO were grown using a directional solidification method under a growth condition recently reported for $Li_xLa_{(1-x)/3}NbO_3$ [21]. The sample is stable in the air with no reaction to moisture. The composition x of the sample was determined as $x = 0.13$ using an inductivity-coupled plasma optical emission spectrometer. The obtained LLTO crystals were cut perpendicular to the growth direction to create a disk with a 20 mm diameter and 1.5 mm thickness. The orientation of each disk was checked in 5 mm steps using an x-ray Laue diffractometer. Six disks consisting of only a single domain with the same crystal orientation were stacked and fixed using hydrogen-free glue (CYTOP). The total weight and volume of the stacked disks were 6.7 g and ~1 cc, respectively. Multiple scattering effect was not considered because the fraction of multiple scattering was as small as 10% estimated by approximating a cylindrical sample shape [22]. Resolution-limited Bragg peaks were confirmed by neutron experiments, which guarantees a bulk single grain of the stacked disk-shape crystals.

All first-principles calculations were conducted within a generalized gradient approximation revised for solids, as developed by Perdew, Burke, and Ernzerhof [23], within the
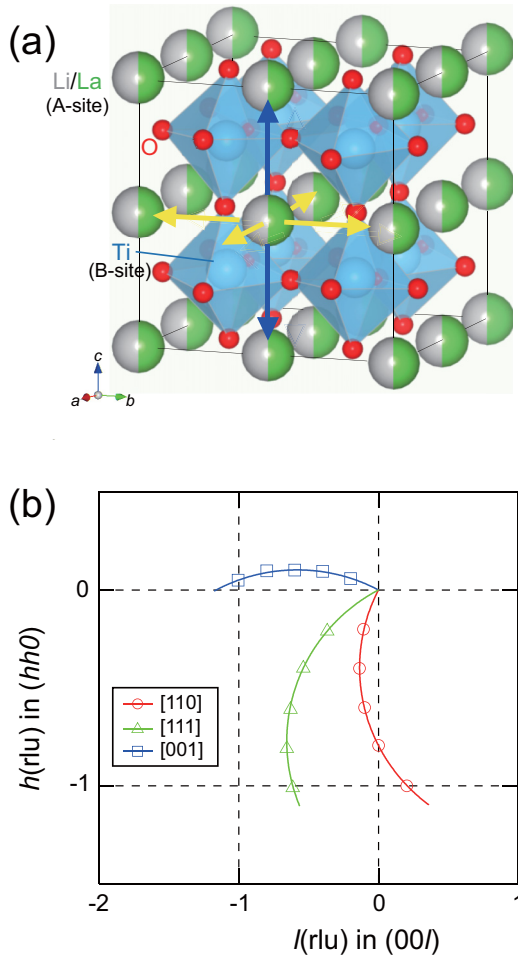

FIG. 1. (a) Crystal structure of LLTO. Arrows in (a) indicate jump vectors of Li$^+$ ions. (b) Scan trajectory of neutron measurements.

framework of the density functional theory [24,25], using the plane-wave basis projector augmented wave (PAW) method [26]. For the PAW potentials, $2s$ and $2p$ electrons for O, $3p$, $3d$, and $4s$ electrons for Ti, and $4f$, $5s$, $5p$, $5d$, and $6s$ electrons for La were explicitly treated as valence electrons, with a plane-wave cutoff energy of 500 eV. Unit cells of the tetragonal $(La_{0.5}, Li_{0.5})TiO_3$ [$(La_1, Li_1)Ti_2O_6$] ($P4/mmm$) structure were assumed and relaxed using a $7 \times 7 \times 4$ k-point mesh within the Brillouin zones generated using the Monkhorst-Pack scheme, and a convergence criterion for residual forces of 0.01 eV/Å. In this study, all first-principles molecular dynamics (FPMD) simulations were performed by Vienna ab initio simulation package (VASP) code [27,28]. Supercells for FPMD simulations for the Li migration trajectory were constructed from $2 \times 2 \times 1$ unit cells of the relaxed tetragonal ($P4/mmm$) structure with one Li vacancy for Li migration. The total number of electrons for the FPMD supercell was adjusted to keep the system insulating. FPMD production runs were performed within the canonical ensemble (constant volume, temperature, and number of atoms) using a Nosé-Hoover thermostat [29] at temperatures (T) of 1000 K, with a time step of 1 fs. The calculated temperature, ion-electron energy, and kinetic energy were stable as a function of the simulation steps, demonstrating the stability of FPMD simulations (Figs. S2–S4 in the Supplemental Material [19]). The structures were relaxed for 2 ps (2000 steps) to ensure that thermodynamic equilibrium had been reached before applying production runs of 40 ps (40 000 steps) for the Li migration trajectory.

QENS measurements were conducted using a time-of-flight near-backscattering spectrometer, DNA installed at the J-PARC MLF [30]. The final neutron energy of 2.08 meV was selected using Si (111) analyzers and a Bragg angle of 87.5°. A pulse shaping chopper rotating at 300 Hz with 3 cm slit provided an elastic resolution of 2.5 μeV and an energy transfer (E) range of $-20 < E < 80$ μeV. Neutron scattering data were obtained using the utsusemi software [31]. The stacked single crystal sample was sealed in an aluminum can with air and mounted to access the (hhl) horizontal scattering plane. There are some controversies in the structure of LLTO. For the high Li-doped sample near $x = 0.13$, tetragonal cell with $a(\sim 2^{1/2}a_p) \times a(\sim 2^{1/2}a_p) \times c(\sim 2a_p)$ [32], where a_p is a lattice parameter of cubic unit cell, simple tetragonal cell with $a(\sim a_p) \times a(\sim a_p) \times c(\sim 2a_p)$ [9], and orthogonal cell with $a(\sim 2a_p) \times b(\sim 2a_p) \times c(\sim 2a_p)$ [11,20] have been proposed. Throughout this paper, we label the momentum transfer in units of the reciprocal lattice vectors $a^* = b^* = 1.147$ Å^{-1} and $c^* = 0.811$ Å^{-1} in the orthogonal notation. Figure 1(b) shows three scan trajectories in the horizontal scattering plane (hhl). The sample was rotated to make scattering trajectories nearly parallel to the three principal axes [110], [111], and [001] below $Q < 1.2$ Å^{-1}. The scattering intensity along the vertical direction was integrated for $-0.2 < k < 0.2$ r.l.u. in $(0, k, -k)$.

III. RESULTS

The QENS spectra at $(-0.8, -0.8, 0)$ at various T's are plotted in the logarithmic scale in Fig. 2. Because Li$^+$ ions are expected to be immobile at $T = 150$ K, we assume that
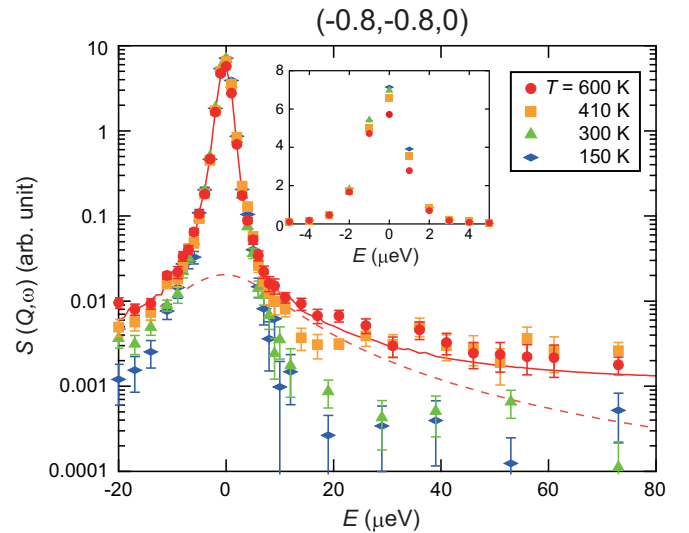

FIG. 2. QENS spectra at $(-0.8, -0.8, 0)$ for ^{7}LLTO measured at $T = 150$, 300, 410, and 600 K. The inset shows enlarged data near $E = 0$ in a linear scale. Scattering intensities for $-0.9 < h < -0.7$ r.l.u. in ($hh0$) are averaged. The solid line indicates a fit with the sum of Lorentzian and delta functions, and a flat background. The $T = 150$ K data were convoluted to the delta and Lorentzian functions as an instrumental resolution. The dotted line represents the Lorentzian function for the fitting to the 600 K data.

the spectrum at $T = 150$ K corresponds to a delta function convoluted with the instrumental resolution. A similar resolution-limited spectrum is also obtained at $T = 300$ K, suggesting that the Li$^+$ ions are still immobile even at $T = 300$ K within the energy or time resolution of the current setup (2.5 μeV ∼ 0.6 GHz ∼ 0.5 ns). At $T \geqslant 410$ K, the intensity of the elastic peak decreases with increasing T (see the inset of Fig. 2), whereas the scattering intensities for $|E| > 4$ μeV are enhanced with T. This suggests the dynamic nature of Li$^+$ ions at $T \geqslant 410$ K. These spectra were fitted with the sum of a Lorentzian and a delta function convoluted with the resolution function estimated from the $T = 150$ K data in addition to a flat background. Although the QENS component, i.e., the Lorentzian component, is 1000 times weaker than the elastic peak, the QENS component, represented by a dotted line in Fig. 2, is clearly extracted, mainly owing to the low background of the DNA spectrometer. Note that the half width at half maximum (Γ) of a Lorentz function was 10 ± 2 μeV, which is comparable to Γ for a sulfide-based Li ionic conductor Li$_7$P$_3$S$_{11}$ obtained using DNA [13].

From the fits at $h = -1.0, -0.8, -0.6, -0.4, -0.2$ (r.l.u.) along the scan trajectory of [110] [Fig. 1(b)], the Q dependence of Γ was obtained at $T = 410$ and 600 K [Fig. 3(a)], where Q is the magnitude of a wave vector from the origin. Because Γ increases quadratically with Q and saturates at a high Q, the obtained result suggests a translational jump diffusion of Li$^+$ for $T \geqslant 410$ K.

In the Chudley-Elliot (CE) model for the translational jump diffusion in Bravais lattices, the scattering function $S(\boldsymbol{Q}, \omega)$ is given by [33]

$$S(\boldsymbol{Q}, \omega) = \frac{\exp(-2W)}{\pi} \frac{\Gamma(\boldsymbol{Q})}{\omega^2 + \Gamma(\boldsymbol{Q})^2}, \qquad (1)$$
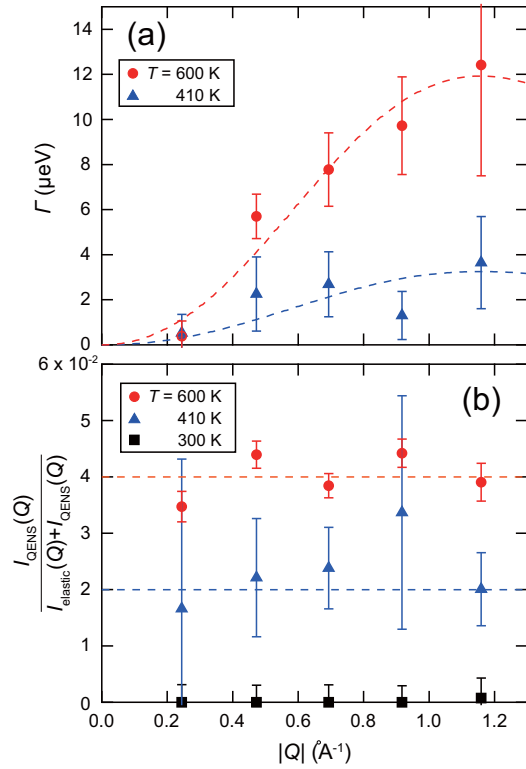
FIG. 3. Q dependences of (a) Lorentzian line width Γ and (b) QENS to total intensity ratio (V_{QENS}) for the [110] scan trajectory, as described in the text. Γ is determined from the data averaged over $\Delta h = \pm 0.1$ r.l.u. in ($hh0$) at approximately $h = -1.0, -0.8, -0.6, -0.4$, and -0.2 r.l.u. The magnitude of a wave vector from the origin Q is calculated at each point and Γ is plotted against Q.

where $\exp(-2W)$ is the Debye-Waller factor. Here, $\Gamma(\boldsymbol{Q})$ is written as

$$\Gamma(\boldsymbol{Q}) = \frac{\hbar}{z\tau} \sum_{j}^{z} [1 - \exp(-i\boldsymbol{Q} \cdot \boldsymbol{l}_j)], \quad (2)$$

where τ is the residence time, $\boldsymbol{l}_j$ is the jump vector, and z is the number of sites. Because $[1 - \exp(-i\boldsymbol{Q} \cdot \boldsymbol{l}_j)] = 0$ when $\boldsymbol{Q} \perp \boldsymbol{l}_j$, $\Gamma(\boldsymbol{Q})$ for the [110] direction reflects the Li$^+$ jumps in the ab plane.

To infer the candidates of the $\boldsymbol{l}_j$ in the ab plane, we conducted MD simulations using first-principles calculations of LLTO. The simulated trajectories of Li$^+$ ions in the La-poor (La2) layer on the ab plane are shown in Fig. 4. For simplicity, we also assumed the absence of La ions at the La2 site in the simulations. Li$^+$ ions move around the A sites, and the trajectories form a square shape with edges toward the a or b directions. The square trajectories are consistent with the distribution of Li$^+$ ions determined from reverse Monte Carlo simulations based on the x-ray and neutron diffraction data [12,13]. Note that some of the Li$^+$ ions jump to the neighboring A site through the bottleneck structure, suggesting that the jump toward the vacant A site is the key pathway of Li$^+$ diffusion.

Based on the information obtained from the MD calculations, Li$^+$ ions are found to jump along the [100] and [010]

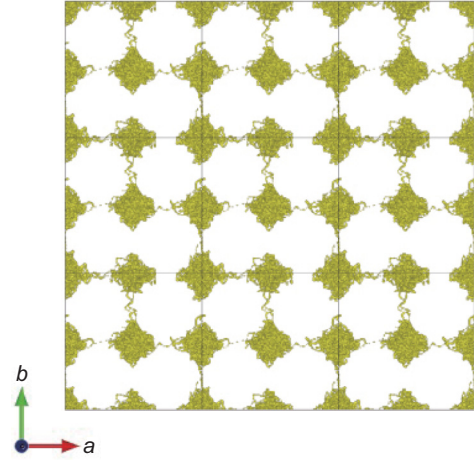FIG. 4. Trajectories of Li$^+$ ions in the ab plane of the La-poor layer simulated by MD using first-principles modeling for LLTO. The yellow traces show trajectories of Li$^+$ ions.

directions in the ab plane. Therefore, Eq. (2) is rewritten as

$$\Gamma(\boldsymbol{Q}) = \frac{\hbar}{2\tau_{ab}} \left[2 - \cos\left(\frac{Q_x l_{ab}}{\sqrt{2}}\right) - \cos\left(\frac{Q_y l_{ab}}{\sqrt{2}}\right) \right]. \quad (3)$$

The observed $\Gamma(\boldsymbol{Q})$ for the [110] direction are reproduced well by this model with $\tau_{ab} = 0.11 \pm 0.01$ ns and $l_{ab} = 3.9 \pm 0.4$ Å, as indicated by the broken lines in Fig. 3(a). Note that the obtained l_{ab} is equivalent to the a-axis length of the cubic perovskite ($a = 3.87$ Å) within the error bar. This is consistent with the result of the MD calculations, in which Li$^+$ ions jump to the neighboring A site through the bottleneck.

For a small Q parallel to the jump vector, Eq. (2) is converted into the following:

$$\Gamma(Q) = \hbar \frac{l_j^2}{2\tau} Q^2 = \hbar D_{\text{Li}} Q^2, \quad (4)$$

where D_{Li} is a self-diffusion coefficient of Li$^+$ ions. Thus D_{Li} is estimated as $6.8 \pm 0.5 \times 10^{-6}$ cm^2/s at $T = 600$ K directly from $l_j^2/2\tau$. Because the jump distance l is roughly independent of T, τ and D_{Li} are easily estimated at $T = 410$ K (see Table II). Inaguma *et al.* reported the thermal activation energy (E_a) of 0.15 eV at above 400 K from the bulk conductivity measurements [5]. The decrease in D_{Li} is in good agreement with the Arrhenius law with E_a of 0.15 eV. It is interesting to compare the present D_{Li} with that for Li$_7$P$_3$S$_{11}$ estimated from the QENS data obtained with DNA: that is, for Li$_7$P$_3$S$_{11}$, $D_{\text{Li}} = 5.7 \times 10^{-6}$ cm^2/s at $T = 473$ K [18]. For LLTO, D_{Li} at $T = 473$ K is estimated from D_{Li} at 600 K and $E_a = 0.15$ eV as $3.1 \pm 0.3 \times 10^{-6}$ cm^2/s, which is close to that for Li$_7$P$_3$S$_{11}$ (Table I). This means that a fast Li$^+$ diffusion is achieved even in oxide-based Li$^+$ ionic conductors, as well as in the sulfide-based conductors, from a microscopic perspective.

In addition to $\Gamma(Q)$, a fraction of the QENS component to the total intensity (V_{QENS}), defined as

$$V_{\text{QENS}} = \frac{I_{\text{QENS}}(Q)}{I_{\text{elastic}}(Q) + I_{\text{QENS}}(Q)}, \quad (5)$$

provides useful information on the Li$^+$ dynamics. Here, $I_{\text{QENS}}(Q)$ and $I_{\text{elastic}}(Q)$ are the integrated intensities of the

TABLE II. Jump distance l, residence time τ, diffusion coefficient D_{Li}, ratio of mobile Li$^+$ ions, and the number of mobile Li$^+$ ions N for LLTO ($x = 0.13$).

Direction	T (K)	l (Å)	τ (ns)	D_{Li} (10^{-6} cm^2/s)	Ratio of mobile Li$^+$ ions (%)	N (10^{27} m^{-3})
[110]	600	3.9 ± 0.4	0.11 ± 0.01	6.8 ± 0.5	50 ± 1	3.35 ± 0.07
[110]	410	3.9 fix	0.42 ± 0.09	1.9 ± 0.1	25 ± 9	1.7 ± 0.6
[001]	600	3.5 ± 0.3	0.14 ± 0.01	4.4 ± 0.3	24 ± 2	1.6 ± 0.2

QENS and elastic signal, respectively. For the translational diffusion, because only the Debye-Waller factor depends on Q in both $I_{QENS}(Q)$ and $I_{elastic}(Q)$, such Q dependence is canceled out. Therefore, V_{QENS} is also independent of Q and is a good indicator for the number of mobile Li$^+$ ions. In fact, V_{QENS} is roughly independent of Q, as shown in Fig. 3(b), which confirms the self-diffusive nature of the observed QENS signal at $T = 600$ K and 410 K. The mobile Li$^+$ ion fraction can be obtained by multiplying V_{QENS} by the ratio of the incoherent scattering cross section σ_{inc} of ^{7}Li to the sum of σ_{inc} from all elements contained in LLTO, as summarized in Table II. The reduction in the fraction of mobile Li$^+$ ions at lower T indicates the decrease in the number of mobile Li$^+$ ions detectable in the time window of the current experimental setup.

Next, to determine the anisotropy of Li$^+$ dynamics, the in-plane ([110])-QENS spectrum is compared with the out-of-plane ([001])-QENS spectrum at the same $|Q| \sim 0.64$ Å^{-1}. Figure 5 shows the spectra measured at $T = 150$ and 600 K. At $T = 600$ K, the [110]-QENS component is similar to the [001]-QENS component, indicating a nearly three-dimensional motion of Li$^+$ ions. In fact, the two QENS spectra are well reproduced by the common Γ of 7 ± 2 μeV, whereas the QENS intensity of the in-plane motion is slightly larger than that of the out-of-plane motion.

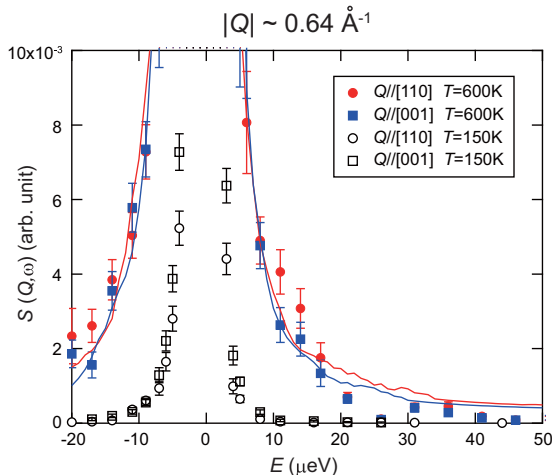FIG. 5. In-plane ([110]) and out-of-plane ([001]) QENS spectra at $|Q| \sim 0.64$ Å^{-1} measured at $T = 150$ and 600 K. To compare the intensity for different directions, neutron transmissions were corrected assuming a rectangular shape of the sample. The in-plane spectra were measured at $(-0.55, -0.55, -0.11)$, whereas the out-of-plane spectra were obtained at $(0.09, 0.09, -0.80)$. The solid lines represent the fits convolved with $T = 150$ K data as instrumental resolution.

Figure 6 shows the $\Gamma(\boldsymbol{Q})$ curves at 600 K along the [110], [001], and [111] directions. For the [001] direction, $\Gamma(\boldsymbol{Q})$ is described as

$$\frac{\hbar}{\tau_c}[1 - \cos(Q_z l_c)], \qquad (6)$$

with $l_c = 3.5$ Å and $\tau_c = 0.14$ ns (Table II). The jump length along the [001] direction (l_c) is close to the a-axis length of the cubic cell, suggesting the jumps between the A sites of the neighboring Li/La planes [Fig. 1(a)]. Because $\tau_{[001]}$ is slightly larger than $\tau_{[110]}$, $D_{Li[001]} < D_{Li[110]}$. The $\Gamma(\boldsymbol{Q})$ curve along the [111] direction is explained well by the coexistence of both jumps in the ab plane and along the c axis using the obtained QENS parameters for each direction.

IV. DISCUSSION

Returning to the Nernst-Einstein equation, D_{Li} is related to the ionic conductivity σ_{Li} as

$$\sigma = e^2 N D / k_B T, \qquad (7)$$

where e is the elementary charge, N is the density of mobile Li$^+$ ions, and k_B denotes the Boltzmann constant. N is estimated as $3.35 \pm 0.07 \times 10^{27}$ m^{-3} from the product of the mobile Li$^+$ ion fraction and the number of Li$^+$ ions ($3x$) per cubic perovskite unit cell 6.7×10^{27} m^{-3} (Table II). The microscopic σ_{Li} (hereafter denoted as σ_{QENS}) at $T = 600$ K is calculated as 0.070 ± 0.006 S/cm and 0.02 ± 0.01 S/cm for the in-plane and out-of-plane directions, respectively. The spatial average of the σ_{QENS} 0.055 ± 0.005 S/cm agrees with that of $\sigma_{Li} \sim 0.1$ S/cm at $T = 600$ K reported from bulk
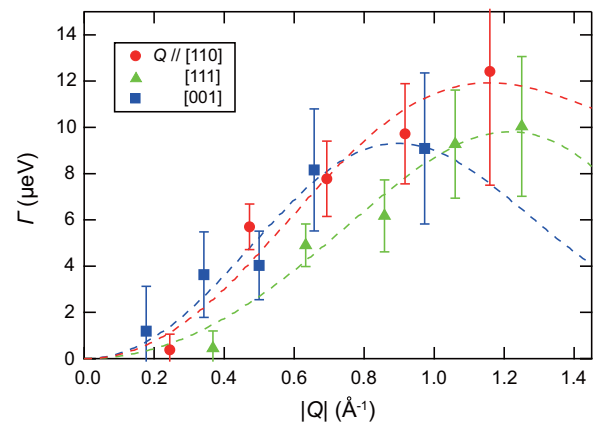

FIG. 6. (a) Q dependences of HWHM Γ of the Lorentzian component along three principal axes [110], [111], and [001] measured at $T = 600$ K.

conductivity measurements for LLTO with slightly lower Li content ($x = 0.11$) [5].

Table I summarizes σ_{Li}, E_a, and D_{Li} for the sulfide-based Li$^+$ ion conductors and LLTO. The σ_{Li} of LLTO is one or two orders of magnitude lower than that of the sulfur-based ones with relatively large E_a. The D_{Li} for LGPS and Li$_7$P$_3$S$_{11}$ are the reported values obtained from pulsed field gradient nuclear magnetic resonance measurements (PFG-NMR), and they are considerably smaller than those of LLTO and Li$_7$P$_3$S$_{11}$ despite their higher conductivity. Presumably, this is because QENS capture the dynamics of the smallest Li dynamic path, whereas PFG-NMR detects dynamics with longer length scale. Comparing the D_{Li} measured by QENS between LLTO and Li$_7$P$_3$S$_{11}$, the fact that D_{Li} for LLTO is comparable to that for Li$_7$P$_3$S$_{11}$, despite the difference in σ_{Li}, leads to the following question: what is the predominant factor for the difference in σ_{Li} between LLTO and Li$_7$P$_3$S$_{11}$? The V_{QENS} for Li$_7$P$_3$S$_{11}$ is 0.23 at $T = 473$ K [34] and the fraction of mobile Li$^+$ ions is 23%, which is similar to that for LLTO (Table II). Then, N is obtained as 3.88×10^{27} m^{-3} by multiplying a Li ion density 1.69×10^{28} m^{-3} for Li$_7$P$_3$S$_{11}$. N for LLTO at $T = 473$ K is 2.2×10^{27} m^{-3}, estimated from a linear interpolation between $T = 410$ and 600 K, which is 1.7 times smaller than that of Li$_7$P$_3$S$_{11}$. Consequently, σ_{QENS} for Li$_7$P$_3$S$_{11}$ is expected to be 3.2 times larger than that for LLTO according to the Nernst-Einstein equation. This is the most reasonable explanation for the difference in σ_{Li} between LLTO and Li$_7$P$_3$S$_{11}$ at the microscopic scale.

Since the discovery of fast Li$^+$ ionic conduction in sulfide-based Li$^+$ ionic conductors [35], sulfide ions are considered to play a significant role in enhancing the mobility of Li$^+$ ions through a large polarization. However, the fact that D_{Li} for LLTO is comparable to that of Li$_7$P$_3$S$_{11}$ indicates the possibility of better oxide-based Li$^+$ ionic conductors by seeking materials with a larger Li density in the unit cell. Regarding the microscopic mechanism of fast Li$^+$ diffusion, a coupling between the rotational motion of the PS$_4^{3-}$ tetrahedra and

σ_{Li} was indicated in the sulfide-based Li$^+$ ionic conductors [36]. In LLTO, structural instabilities of the tilting modes of TiO$_6$ tetrahedra are suggested from first-principles calculations [37]. Further studies on the dynamics of the host lattice of Li$^+$ ionic conductors will be required to understand the mechanism of fast Li$^+$ ionic conduction in solids.

V. CONCLUSION

We studied the dynamics of Li$^+$ ions in a solid-state electrolyte LLTO ($x = 0.13$) using QENS and first-principles MD simulations. We observed clear QENS signals along the three principal axes [110], [111], and [001] at $T = 600$ K by using the large ^{7}Li-enriched single crystal. Directional information of the Li$^+$ jump, such as the residence time and jump vector determined at the microscopic scale, reveals the dynamical conduction paths of Li$^+$ ions: jumps of Li$^+$ ions to the neighboring *A* site through the bottleneck structure, which are supported by the first-principles MD simulations. The self-diffusion coefficients of Li$^+$ ions are found to be quasi-isotropic, suggesting the nearly three-dimensional diffusion of Li$^+$ ions. Furthermore, the estimated self-diffusion coefficients of Li$^+$ are comparable to those of the sulfide-based Li$^+$ ion conductor Li$_7$P$_3$S$_{11}$, although the ionic conductivity of LLTO is 10 times smaller than that of Li$_7$P$_3$S$_{11}$. This microscopic information on Li$^+$ diffusion can provide a way to increase Li$^+$ ionic conductivity in oxide-based solid electrolytes.

[1] J. M. Tarascon and M. Armand, Nature (London) **414**, 359 (2001).

[2] M. Armand and J.-M. Tarascon, Nature (London) **451**, 652 (2008).

[3] N. Kamaya, K. Homma, Y. Yamakawa, M. Hirayama, R. Kanno, M. Yonemura, T. Kamiyama, Y. Kato, S. Hama, and K. Kawamoto, Nat. Mater. **10**, 682 (2011).

[4] L. Latie, G. Villeneuve, D. Conte, and G. Le Flem, J. Solid State Chem. **51**, 293 (1984).

[5] Y. Inaguma, C. Liquan, M. Itoh, T. Nakamura, T. Uchida, H. Ikuta, and M. Wakihara, Solid State Commun. **86**, 689 (1993).

[6] Y. Inaguma, J. Ceram. Soc. Jpn. **114**, 1103 (2006).

[7] J. L. Fourquet, H. Duroy, and M. P. Crosnier-Lopez, J. Solid State Chem. **127**, 283 (1996).

[8] Y. Harada, T. Ishigaki, H. Kawai, and J. Kuwano, Solid State Ionics **108**, 407 (1998).

[9] J. Ibarra, A. Várez, C. León, J. Santamaría, L. M. Torres-Martínez, and J. Sanz, Solid State Ionics **134**, 219 (2000).

[10] D. Mazza, S. Ronchetti, O. Bohnké, H. Duroy, and J. L. Fourquet, Solid State Ionics **149**, 81 (2002).

[11] Y. Inaguma, T. Katsumata, M. Itoh, Y. Morii, and T. Tsurui, Solid State Ionics **177**, 3037 (2006).

[12] K. Ohara, A. Kawakita, L. Pusztai, L. Temleitner, S. Kohara, N. Inoue, and S. Takeda, J. Phys.: Condens. Matter **22**, 404203 (2010).

[13] K. Mori, S. Tomihira, K. Iwase, and T. Fukunaga, Solid State Ionics **268**, 76 (2014).

[14] A. Kuhn, V. Duppel, and V. B. Lotsch, Energy Environ. Sci. **6**, 3548 (2013).

[15] A. Hayashi, S. Hama, H. Morimoto, M. Tatsumisago, and T. Minami, J. Am. Ceram. Soc. **84**, 477 (2001).

[16] H. Stöffler, T. Zinkevich, M. Yavuz, A. Senyshyn, J. Kulisch, P. Hartmann, T. Adermann, S. Randau, F. H. Richter, J. Janek *et al.*, J. Phys. Chem. C **122**, 15954 (2018).

[17] Y. Onodera, K. Mori, T. Otomo, M. Sugiyama, and T. Fukunaga, J. Phys. Soc. Jpn. **81**, 044802 (2012).

[18] K. Mori, K. Enjuji, S. Murata, K. Shibata, Y. Kawakita, M. Yonemura, Y. Onodera, and T. Fukunaga, Phys. Rev. Appl. **4**, 054008 (2015).

[19] See Supplemental Material at http://link.aps.org/supplemental/10.1103/PhysRevB.104.094305 for the details of the powder x-ray diffraction and the stability of FPMD simulations, which includes Refs. [11] and [20].

[20] H.-T. Chung and D.-S. Cheong, Solid State Ionics **120**, 197 (1999).

[21] Y. Fujiwara, K. Hoshikawa, and K. Kohama, J. Cryst. Growth **433**, 48 (2016).

[22] I. A. Blech and B. L. Averbach, Phys. Rev. **137**, A1113 (1965).

[23] J. P. Perdew, K. Burke, and M. Ernzerhof, Phys. Rev. Lett. **77**, 3865 (1996).

[24] P. Hohenberg and W. Kohn, Phys. Rev. **136**, B864 (1964).

[25] W. Kohn and L. J. Sham, Phys. Rev. **140**, A1133 (1965).

[26] P. E. Blöchl, Phys. Rev. B **50**, 17953 (1994).

[27] G. Kresse and J. Furthmüller, Phys. Rev. B **54**, 11169 (1996).

[28] G. Kresse and D. Joubert, Phys. Rev. B **59**, 1758 (1999).

[29] D. J. Evans and B. L. Holian, J. Chem. Phys. **83**, 4069 (1985).

[30] K. Shibata, N. Takahashi, Y. Kawakita, M. Matsuura, T. Yamada, T. Tominaga, W. Kambara, M. Kobayashi, Y. Inamura, T. Nakatani, K. Nakajima, and M. Arai, JPS Conf. Proc. **8**, 036022 (2015).

[31] Y. Inamura, T. Nakatani, J. Suzuki, and T. Otomo, J. Phys. Soc. Jpn. **82**, SA031 (2011).

[32] A. Várez, F. García-Alvarado, E. Morán, and M. A. Alario-Franco, J. Solid State Chem. **118**, 78 (1995).

[33] R. Hempelmann, *Quasielastic Neutron Scattering and Solid State Diffusion* (Clarendon Press, Oxford, 2000).

[34] K. Mori (personal communication).

[35] R. Kanno, T. Hata, Y. Kawamoto, and M. Irie, Solid State Ionics **130**, 97 (2000).

[36] J. G. Smith and D. J. Siegel, Nat. Commun. **11**, 728 (2020).

[37] H. Moriwake, X. Gao, A. Kuwabara, C. A. J. Fisher, T. Kimura, Y. H. Ikuhara, K. Kohama, T. Tojigamori, and Y. Ikuhara, J. Power Sources **276**, 203 (2015).

[38] K. Momma and F. Izumi, J. Appl. Crystallogr. **44**, 1272 (2011).